applied optics

Improved identification of the solution space of aerosol microphysical properties derived from the inversion of profiles of lidar optical data, part 3: case studies

Alexei Kolgotin,[1,6] Detlef Müller,[2,3,*] ⓘ Eduard Chemyakin,[2] Anton Romanov,[4] and Valentin Alehnovich[5]

[1]*Physics Instrumentation Center, Moscow 142190, Russia*
[2]*Science Systems and Applications, Inc. (SSAI), NASA LaRC, 1 Enterprise Parkway, Hampton, Virginia 23666, USA*
[3]*University of Hertfordshire, Hatfield, Hertfordshire AL10 9AB, UK*
[4]*The National University of Science and Technology, Leninskii av. 4, Moscow 119049, Russia*
[5]*Bauman Moscow State Technical University, 2nd Baumanskaya str. 5, Moscow 105005, Russia*
[6]*e-mail: alexeift@yahoo.com*
*Corresponding author: d.mueller@herts.ac.uk

We conclude our series of publications on the development of the gradient correlation method (GCM), which can be used for an improved stabilization of the solution space of particle microphysical parameters derived from measurements with multiwavelength Raman and high-spectral-resolution lidar (3 backscatter +2 extinction coefficients). We show results of three cases studies. The data were taken with a ground-based multiwavelength Raman lidar during the Saharan Mineral Dust Experiment in the Cape Verde Islands (North Atlantic). These cases describe mixtures of dust with smoke. For our data analysis we separated the contribution of smoke to the total signal and only used these optical profiles for the test of GCM. The results show a significant stabilization of the solution space of the particle microphysical parameter retrieval on the particle radius domain from 0.03 to 10 μm, the real part of the complex refractive index domain from 1.3 to 1.8, and the imaginary part from 0 to 0.1. This new method will be included in the Tikhonov Advanced Regularization Algorithm, which is a fully automated, unsupervised algorithm that is used for the analysis of data collected with the worldwide first airborne 3 backscatter +2 extinction high-spectral-resolution lidar developed by NASA Langley Research Center.

OCIS codes: (010.1110) Aerosols; (010.3640) Lidar.

https://doi.org/10.1364/AO.57.002499

1. INTRODUCTION

In [1,2] we presented the theoretical framework and simulation results obtained with the gradient correlation method (GCM). This novel method has been specially designed for acquiring more stable retrieval results of particle microphysical parameters (PMPs) from the inversion of backscatter and extinction coefficients measured with multiwavelength Raman and high-spectral-resolution lidar at the wavelengths $\lambda = 355$, 532, and 1064 nm. In this last paper on the development and testing of GCM, we will present results of case studies based on experimental data.

We selected three cases for this test: the data were taken with a ground-based multiwavelength Raman lidar on 22 Jan 2008, 31 Jan 2008, and 3 Feb 2008 during the Saharan Mineral Dust Experiment (SAMUM) in the Cape Verde Islands (North Atlantic) [3]. These measurement cases describe mixtures of dust with smoke. For our data analysis we separated the contribution of smoke to the total optical signal and only used optical data (OD) of these profiles for the test of GCM [4].

We summarize the main points of the methodology in Section 2. We present the case studies in Section 3. We discuss the results in Section 4. Section 5 concludes our data analysis

and discussion of results. The Appendix A lists the abbreviations used in this paper.

2. METHODOLOGY

In the following we briefly summarize the methodology. This novel method has been specially designed for acquiring more stable retrieval results of PMPs from inversion of OD (g) of backscatter (β) and extinction (α) coefficients measured with multiwavelength Raman and high-spectral-resolution lidar at the wavelengths $\lambda = 355$, 532, and 1064 nm.

The PMP set (p) includes the mean radius (r_{mean}) and effective radius (r_{eff}); mean width, that is, geometrical standard deviation (σ) of a particle size distribution ($f(r)$), and number (n), surface-area (s), and volume (v) concentrations, as well as the real (m_R) and imaginary (m_I) parts of the complex refractive index (CRI) $m = m_R - im_I$. The CRI is the most important data product in our development work as this parameter allows us to infer the light-absorption characteristics of particle pollution.

These parameters follow from solving Fredholm integral equations of the first kind,

$$\int_{r_{min}^{(l)}}^{r_{max}^{(l)}} K_g(\lambda, m^{(l)}, r) f^{(l)}(r) dr = g^{(l)}(\lambda),$$
$$l = 1, ..., N_L; g = \alpha, \beta, \tag{1}$$

where $K_g(\lambda, m^{(l)}, r)$ is the kernel function. The particle radius is defined as $r \in [r_{min}^{(l)}, r_{max}^{(l)}]$. In the case of spherical particle geometry the optical properties of particles can be described by Mie scattering theory [5]. The superscript l indicates the number of the height bins of the measured optical profiles and also describes the height bins of the profiles of the PMPs. The total number of height bins is N_L.

Solving Eq. (1) for the microphysical parameters is an ill-posed problem, which means the solution space is nonunique, oscillating, and sensitive to measurement errors. The ill-posed problem can be solved with different approaches as shown in, for instance, [6–10]. All these approaches have one feature in common: they provide us with an extended solution space $F^{(l)} = \{f_1^{(l)}(r), ..., f_{Nsol}^{(l)}(r)\}$ [2] in the sense that we obtain a large number of individual solutions N_{sol}, which however often contain a significant number of mathematically correct but physically meaningless solutions. The parameter N_{sol} depends on particle radius in the domain $r \in [r_{min}^{(l)}, r_{max}^{(l)}]$ and the CRI in the domain $m_R \in [m_{R,min}^{(l)}, m_{R,max}^{(l)}]$ and $m_I \in [m_{I,min}^{(l)}, m_{I,max}^{(l)}]$. The domains of particle radius and CRI are tested for potential solutions. The number of solutions can reach 10^5 and more. This number is based on the domains we chose for our inversion algorithm. Even if we use advanced regularization algorithms [11,12], including Tikhonov regularization [13], there is no guarantee that the final solution space $F^{(l)}$ will be stable and physically meaningful.

In view of these problems we specifically designed GCM to find a more stable and constrained final solution-space from the initial solution space $F^{(l)}$. The main idea of GCM is that we select individual solutions $f_j^{(l)}(r), j = 1, ..., N_{sol}$, that fulfill the constraints

$$|[a_p \alpha^{(l)}(355) + b_p] - p_j^{(l)}| < \delta p \quad p = s, v/r_{eff}, n(r_{mean}^2 + \sigma^2), \tag{2a}$$

$$|[a_p \mathring{a}_\alpha^{(l)} + b_r] - p_j^{(l)}| < \delta p \quad p = r_{eff}, \tag{2b}$$

$$|[a_p r_{eff,j}^{(l)} + b_p] - p_j^{(l)}| < \delta p \quad p = r_{mean}, \sigma. \tag{2c}$$

The parameter $\mathring{a}_\alpha^{(l)}$ denotes the extinction-related Ångström exponent (EAE), a_p and b_p denote the regression coefficients (RCs), and δp denotes the threshold [1,2]. The final solution f_{av} then follows from averaging the selected individual solutions $f_j^{(l)}(r)$ [7].

The EAE in Eq. (2) follows from the lidar measurements. The individual PMPs $p_j^{(l)}$ are defined by the respective particle size distribution (PSD) $f_j^{(l)}(r)$. The threshold δp is chosen such that it usually does not exceed 20%. The RCs follow from the methodology presented in [1,2]. For instance, in the case of Eq. (2a) the RCs can be estimated to better than 20% for any type of PSD, including mono-and bimodal distributions {see intervals (18a) in [1]}. In the case of Eqs. (2(b) and (2(c) the RC intervals are broader and strongly depend on the modality of the PSDs; see Table 4 in [2] for monomodal PSDs.

A careful estimation of the RCs is needed to keep GCM robust. Thus, we also developed *proximate analysis* (PA). PA is based on using a look-up table (LUT) of optical data and their respective microphysical parameters and comparing its elements to data taken with lidar [2]. The LUT consists of 63,869 OD sets of $3\beta + 2\alpha$ coefficients and their respective lidar data products (LDPs) such as EAE, $\mathring{a}_\alpha$; backscatter-related Ångström exponent (BAE), $\mathring{a}_\beta$; and lidar ratio (LR) α/β. The entries in the LUT were calculated from

- 221 different logarithmic-normal monomodal PSDs that cover a range of effective radius from 0.02 to 3 μm,
- 289 combinations of CRI with real parts belonging to the interval [1.3, 1.7] and imaginary parts belonging in the interval [0, 0.05].

We consider this LUT as an etalon (standardized) solution space F which can be used for the classification of aerosol types; see for example Table 1 in [1]. This reference solution space can also be used for the analysis of the modality of PSDs. Besides that, the LUT allows us to carefully estimate the CRI of monomodal PSDs if BAE, EAE, LRs at two wavelengths, and effective radius are available [1].

3. CASE STUDIES

A. Measurement Case from 31 January 2008

The OD set was taken on Jan 2008 during SAMUM [3]. A mixed dust–smoke plume was observed. The OD were separated into the contribution by the smoke particles and the contribution by the dust particles; see [4]. We analyzed the part belonging to the biomass-burning particles.

Figure 1 shows the profiles of the backscatter and extinction coefficients ($3\beta + 2\alpha$) and the profiles of the LRs, BAEs, and EAE. The profiles consist of $N_L = 12$ height bins. We processed the OD sets of each height bin between 1.5 and 5.0 km in the way described in Section 3 in [2].
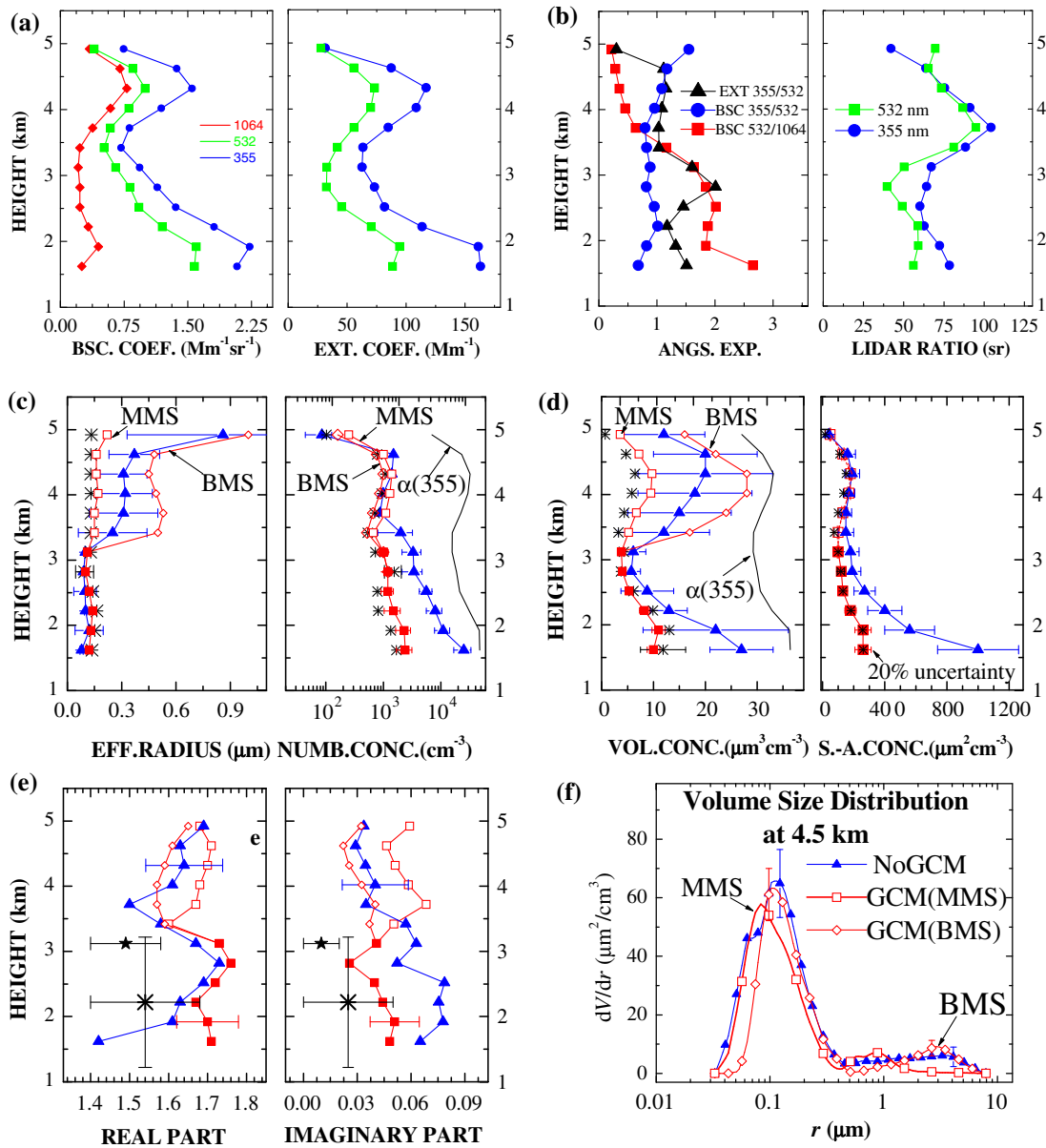
Fig. 1. Experimental data taken on 31 January 2008. (a) Backscatter coefficients at 355, 532, and 1064 nm, and extinction coefficients at 355 and 532 nm. (b) BAE, EAE, and LRs. (c)–(f) Retrieved PMP (effective radius, number, surface-area, and colume concentration), CRI (real and imaginary part), and PSD. The results were obtained without the use of GCM (NoGCM, triangle), with the use of GCM under the assumption that the PSDs are monomodal (MMS, squares) or bimodal (BMS, diamonds). We used the value $a_s = 1.6$. The asterisks denote the results from our proximate estimation of the fine-mode parameters. The stars describe the results of the CRI of the fine-mode particles. We obtained these results from combining PA with the results for effective radius. Effective radius was obtained from using GCM.

1. Proximate Analysis of Particle Parameters

We classified the particles according to Table 1 in [1]. The lower part of the profile, $l = 1 - 6$, is represented by the aerosol particle cases 8 and 9. The upper part of the profile, $l = 7 - 12$, is represented by the aerosol particle cases 1, 2, and 5 (see Table 1). That means that small particles accumulated at 1.5–3 km height, and the share of larger particles increased in the height range from 3 to 5 km. The aerosol case 2 (from 4.0 to 4.5 km height) may include either small particles with strong light-absorption capacity or very large particles of the coarse mode of bimodal PSDs.

We used simplified PA to make an initial assumption about the modality of the investigated PSDs and checked if the values of the LDP from our LUT were close to the values obtained from the lidar measurements. In the first step of our analysis we found the minimal discrepancy $\rho_{LUT,f}$ for the OD sets of each height bin according to Eq. (32) in [2]. Table 2 shows that the minimum discrepancy increases from $\rho_{LUT,f} = 2.7\%$ at $l = 7$ (3.5 km) to 18.6% at $l = 12$ (5 km) and 20.2% at $l = 1$ (1.5 km).

The relatively larger discrepancies in the lowest and uppermost parts of the profiles indicate larger measurement errors or/and that the PSDs are bimodal below 3 km and above

Table 1. Number of Aerosol Cases Presented in Table 1 of [1] Versus Height Bin Number *l* and Date of Measurement

l	31 Jan 2008	3 Feb 2008	22 Jan 2008
1	9	8	5
2	8	5	5
3	8	6	5
4	8	6	5
5	9	5	2
6	9	5	2
7	5	2	2
8	5	2	no data
9	2	2	
10	2	2	
11	2	2	
12	1	6	

3.5 km, respectively. To check this latter assumption we determined in the next step of our simplified PA the discrepancy $\rho_{\mathrm{LUT},c}$ at each height bin (see Table 2) according to Eq. (31) in [2]. With regard to the layers in the lower part of the profiles (1.5–3 km height) we find the following results: in one of the cases the $\rho_{\mathrm{LUT},c}$ takes into account the fractions φ_g that do not fulfill Eq. (30) in [2]. In the other cases the values of $\rho_{\mathrm{LUT},c}$ are considerably higher and significantly exceed the value of $\rho_{\mathrm{LUT},f}$. Therefore, our attempt of splitting the OD into a fine mode and a coarse mode fails in the height range from 1.5 to 3 km. However, the value of $\rho_{\mathrm{LUT},c}$ decreases above 3 km. The value varies between 7.0 and 16.4% and becomes even less than the values of $\rho_{\mathrm{LUT},f}$ at and above $l = 9$ (4 km).

Based on our simplified PA we can draw the following conclusions:

- the PSD is monomodal below 3 km,
- effective radius below 3 km is less than 0.3 µm. Furthermore, effective radius is less than 0.12 µm at $l = 1$, 5, 6 (see cases 8 and 9 of Table 1 in [1]), and
- we cannot rule out that the PSDs are bimodal above 3 km height.

Table 2. Measurement from 31 January, 2008[a]

			$\varphi_{\alpha(355)}$	
			Fitted from	**Minimization of**
l	$\rho_{\mathrm{LUT},f}$	$\rho_{\mathrm{LUT},c}$	**Eq. (23) in [2]**	**Eq. (31) in [2]**
1	20.2%	—	1	1
2	13.0%	—	1	1
3	11.3%	—	1	1
4	11.9%	—	1	1
5	7.5%	—	1	1
6	6.1%	—	1	1
7	2.7%	7.0%	0.74	0.70
8	7.3%	8.0%	0.74	0.60
9	12.2%	9.2%	0.77	0.80
10	15.5%	7.0%	0.80	0.80
11	16.4%	16.4%	0.78	0.90
12	18.6%	9.2%	0.30	0.55

[a]We show the discrepancies $\rho_{\mathrm{LUT},f}$ and $\rho_{\mathrm{LUT},c}$ introduced in Eqs. (32) and (31) in [2], respectively. Also shown are the fine-mode fractions derived from our linear regression analysis according to Eq. (23) and estimated by our minimization procedure according to Eq. (31) in [2] versus height bin number *l*.

In the next step of our analysis we used our PA to estimate the particle parameters of the PSD. The PSD is monomodal below 3 km height, and the fine mode coincides with the total PSD. The EAE belongs to the interval $\mathring{a}_\alpha \in [1, 2]$, and we can immediately use Eqs. (13)–(15) and (24d,e) in [2] for estimating effective radius, surface area, volume, and number concentrations in these height levels. The results of the calculations are shown in Figs. 1(c)–1(e) as asterisks. We see that effective radius varies within 0.10–0.16 µm, and surface-area, volume, and number concentrations vary within 100–260 µm² cm⁻³, 4–14 µm³ cm⁻³, and 725–1680 cm⁻³, respectively.

Our simplified PA shows that bimodal PSDs may be present above 3 km height. Therefore, we use Eqs. (23) and (24) in [2] for estimating the microphysical parameters of the fine-mode fraction of the PSD in the upper part of the profile. These equations require the assessment of the fine-mode fraction $\varphi_{\alpha(355)}^{(l)}$ ($l = 7, …, 12$). We fit that parameter such that we keep the fine-mode EAE close to $\mathring{a}_{\alpha,f} = 1.55 – 1.60$ in Eq. (23) of [2]. The choice of $\mathring{a}_{\alpha,f} = 1.55 – 1.60$ allows us to test if the lower and the upper parts of the aerosol profiles contain particles in the fine-mode fraction with similar sizes. Figure 1(b) shows that the EAE varies between 1.2 and 2.0. The average value is 1.51 in the lower part of the profile (from 1.5 to 3 km). The EAE is 1.6 at 3 km height. If we use $\mathring{a}_{\alpha,f} = 1.55 – 1.60$ in Eq. (23) of [2] for the height range above 3 km, we find the following result: the fine-mode fraction changes from $\varphi_{\alpha(355)}^{(12)} = 0.3$ at $l = 12$ to $\varphi_{\alpha(355)}^{(7)} = 0.74$ at $l = 7$ (see Table 2).

Table 2 shows the comparison of the fine-mode particle parameters that we obtain from applying the fitting procedure according to Eq. (23) in [2] and from applying the minimization procedure according to Eq. (31) in [2]. The difference does not exceed 15% in the height bins $l = 7 – 11$. The only exception is the uppermost height bin, $l = 12$, where the difference reaches 45%. The low discrepancy between the results obtained with the two methods corroborates our initial assumptions, namely,

- the PSD is bimodal above 3 km, and
- the fine-mode particles above 3 km and below 3 km height are similar in size.

We calculated effective radius, surface-area and volume concentrations, and the lower and upper limits of number concentration of the fine-mode particles in the upper part of the profile. For these calculations we used all the values $\varphi_{\alpha(355)}^{(l)}$ we derived from Eq. (23) in [2]. We used Eqs. (24a), (24b), (24c), (24d), and (24e) in [2]. The results of the calculations are shown in Figs. 1(c) and 1(d) as asterisks. We see that effective radius is constant and equal to 0.13 µm. Surface-area, volume, and number concentrations vary within 15–150 µm² cm⁻³, 1–6 µm³ cm⁻³, and 102–1075 cm⁻³, respectively.

We can also use PA for estimating the CRI in the lower part of the profile since that part only consists of a monomodal PSD. Unfortunately, even a narrow interval of the discrepancy, namely, $[\rho_{\mathrm{LUT},f}^{(l)}, \rho_{\mathrm{LUT},f}^{(l)} + 1\%]$, $l = 1, …, 6$, results in a wide spread of the real and imaginary parts of the CRI from 1.4 to 1.675 (real part) and from 0.001 to 0.05 (imaginary part) [see

asterisk on Fig. 1(e). We investigated the reasons for the CRI uncertainty in [14]. The reasons are typical for small particles.

2. Gradient Correlation Method for the Retrieval of Particle Parameters

We used GCM (see Section 3.B.1 in [2]) for the retrieval of the PMPs. We summarize the most important details.

We generate the solution space $F^{(l)}$ for all height bins $l = 1, \ldots, 12$ [7]. Each solution space $F^{(l)}$ contains about 10^5 individual solutions, which are retrieved by using the 150 inversion windows that are in the radius range from 0.03 to 10 μm. We used 20 equidistant values of the real part, that is, $m_R \in [1.325, 1.8]$, and 30 equidistant values of the imaginary part, that is, $m_I \in [0.0, 0.1]$. The solution spaces then are postprocessed by using the constraints specifically developed for GCM and described by Eq. (2).

Two strategies are used in this step. One of the strategies assumes that the PSD is monomodal (MMS). The other strategy assumes that the PSD is bimodal (BMS). BMS may mean that either only big particles are present or that the PSD is a composition of both big and small particles.

For comparison of the quality of the results we also use our software as if it were operated in an automated, unsupervised mode [15]; that is, in that case we would not use any constraints on the parameters r_{eff} and n; instead we would use

$$r \in [0.03, 10], \tag{3a}$$

$$m_R \in [1.325, 1.8], \tag{3b}$$

$$m_I \in [0.0, 0.1]. \tag{3c}$$

In the following we denote this traditional approach as NoGCM.

The results retrieved with NoGCM (blue curve with triangles), with GCM using MMS (red curve with squares), and with CGM using BMS (red curve with diamonds) are shown in Figs. 1(c)–1(f). The statistics for all retrieval results are presented in Fig. 2.

As can be seen, the use of NoGCM leads to unrealistically large values of number concentration (2×10^4 cm^{-3}). Surface-area concentration also shows rather unrealistic values (10^3 μm^2 cm^{-3}) in the lower part of the profile (<3 km). Simultaneously, we find very high RCs of $a_s = 5.5$ [Fig. 2(b)], $a_v = 1.87$ [Fig. 2(c)], and $a_n = 0.46$ [Fig. 2(d)]. These numbers confirm that the profiles of s and n might contain outliers. Besides that, the correlation coefficients are low ($R^2 = 0.66 - 0.84$). We know this effect (outliers of the number concentration) very well from nearly 20 years of experience in the development of data inversion methods. Until now, the most efficient way to suppress these outliers was to increase r_{min} from 0.03 to 0.05–0.075 μm in the particle radius domain given by Eq. (3a).

However, Fig. 2(a) shows that we can distinguish between two separate aerosol fractions. One of these fractions is characterized by a small effective radius of approximately 0.1 μm and $å_\alpha > 1.3$. This fraction appears in the lower part of the aerosol profile. The other fraction includes larger particles with an effective radius larger than 0.25 μm and $å_\alpha < 1.3$. This second fraction appears in the upper part of the aerosol profile.
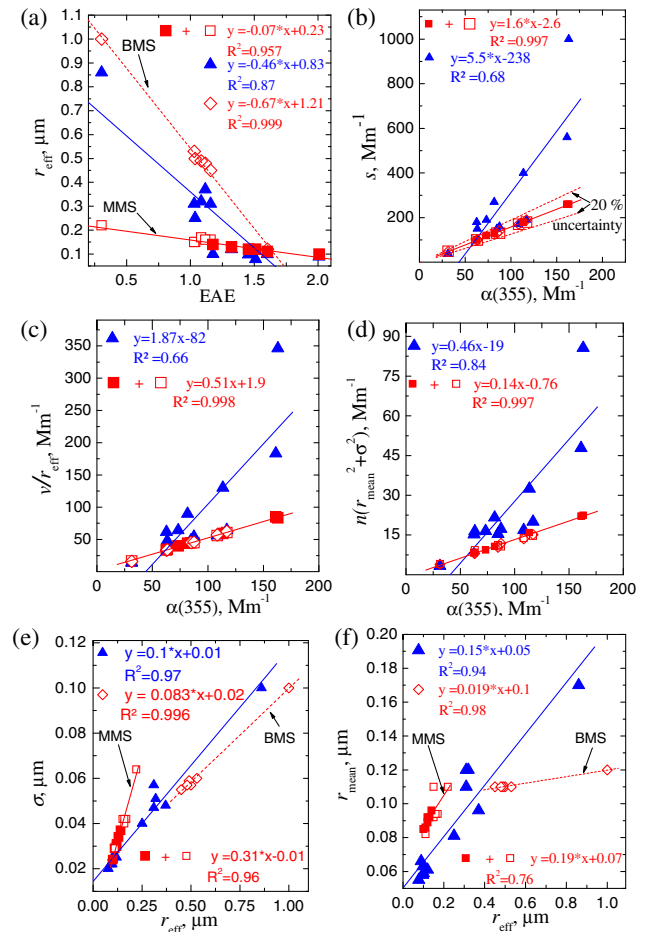

Fig. 2. Statistics of the experimental data (EAE and extinction coefficient at 355 nm) and the PMPs for the measurement case from 31 January 2008. The results were obtained without the use of GCM (NoGCM, triangles), and with the use of GCM and the assumption that the PSDs are monomodal (MMS, squares) or bimodal (BMS, diamonds), respectively. We used the value $a_s = 1.6$. The solid lines describe the correlation trends according to the equation $y = ax + b$. Information on the regression parameters and the correlation coefficient R^2 is given in the legends of each subfigure.

For that reason we split the OD profile into a lower (from 1.5 to 3.0 km, $l = 1, \ldots, 6$) and an upper part (from 3.0 to 5.0 km, $l = 6, \ldots, 12$) and treat both parts independently of each other in our data analysis. For the postprocessing procedure of the lower part of the profile we used only MMS; see Section 3.A.1 and closed squares in Fig. 2. With regards to the upper part of the profile we used MMS (open squares) and BMS (diamonds). The RCs used for all cases are listed in Table 3. We chose them in the way described in Section 3.B.1 in [2].

We find a significant stabilizing effect for number and surface-area concentrations. The values of both parameters decrease by one-and-a-half orders of magnitude in the height range from 1.5 to 3.0 km compared to the results obtained with NoGCM. Simultaneously, the correlation coefficients are close to 1. We also find a stabilization of the solution space of volume concentration in the lowest height bins. The value for volume concentration drops from 27 to 11 μm^3/cm^3. However, in upper height levels the volume concentration

Table 3. Measurement from 31 January 2008[a]

p	a_p	b_p	δp	a_p	b_p	δp
	MMS (1.5–5.0 km)			BMS (3.0–5.0 km)		
s	1.6	0	10%	1.6	0	10%
v/r	0.53	0	10%	0.53	0	10%
$n(r_{mean}^2 + \sigma^2)$	0.127	0	10%	0.127	0	10%
r_{eff}	−0.08	0.26	0.05 μm	−0.65	1.2	0.1 μm
σ	0.25	0	25%	0.09	0.02	20%
r_{mean}	0.3	0.06	20%	0.016	0.1	20%

[a]Shown are the regression coefficients and thresholds that were used as constraints in GCM.

increases from 20 to 30 $\mu m^3/cm^3$ if we use BMS. As a result, effective radius increases approximately twofold in these heights compared to the results we obtain from using NoGCM.

We note that our PA of the fine-mode PMPs and the results we obtain with MMS are comparably close to each other. Simultaneously, Fig. 1(f) shows that the fine modes of the PSDs retrieved with BMS and MMS are close to each other at 4.5 km height as well. For that reason we believe that even if our MMS assumption is wrong, we can expect that the parameters that describe the fine mode of the retrieved PMPs are comparably accurate. PSDs retrieved with GCM for different height bins are shown in Fig. 8(a).

With regards to the retrieval of the CRI we find that the column-averaged values obtained with NoGCM and GCM are close to each other. We find values of $m_R = 1.6 - 1.7$ and $m_I = i0.04 - i0.05$. We believe that the CRI is overestimated. This effect has also been observed in simulations with synthetic OD.

In another step of our analysis we combined PA and the results we obtained for effective radius from using GCM. The goal of this step was to obtain a better estimate of the CRI. We considered a height layer where it is certain that the PSD is monomodal and the discrepancy $\rho_{LUT,f}$ is as small as possible along the aerosol profile. In that case the most appropriate layer is the layer described by height bin $l = 6$, which contains aerosol particles described by case 9 (see Table 1 in [1]). In that case, the $\rho_{LUT,f}$ is equal to 6.1% (see Table 2).

Effective radius retrieved with GCM is $r_{eff}^{(6)} = 0.11$ μm in height bin $l = 6$ [see Fig. 1(c)]. We find a solution space in our LUT for which the discrepancy,

$$\rho_{LUT} = \frac{1}{6}\sum_p \rho_p,$$

$$p = \mathring{a}_\alpha, \mathring{a}_{\beta(355),\beta(532)}, \mathring{a}_{\beta(532),\beta(1064)}, \frac{\alpha(355)}{\beta(355)}, \frac{\alpha(355)}{\beta(355)}, r_{eff}, \quad (4)$$

does not exceed $\rho_{LUT} = 11\%$. The expression

$$\rho_p = |p_{LUT} - p_{experiment}|/p_{LUT} \times 100\%$$

in Eq. (4) describes the individual discrepancies between experimental data (measured or retrieved) and data in the LUT for each parameter p.

Table 4 presents the data in our LUT that fulfill the condition $\rho_{LUT} \leq 11\%$. The table contains values of the real and imaginary parts derived from the solution space, and values of the total (ρ_{LUT}) and the individual (ρ_p) discrepancies [see meaning of p in Eq. (4)] of all solutions. Table 4 shows that

Table 4. Measurement from 31 January 2008[a]

		Individual Discrepancies ρ_p for:						
m_R	m_I	BAE1	BAE2	$\mathring{a}_\alpha$	$\frac{\alpha(355)}{\beta(355)}$	$\frac{\alpha(532)}{\beta(532)}$	r_{eff}	ρ_{LUT}
1.400	0.00E + 00	29%	11%	7%	1%	8%	3%	10%
1.400	5.00E − 04	29%	12%	7%	0%	9%	3%	10%
1.400	1.00E − 03	28%	12%	7%	1%	10%	3%	10%
1.400	2.00E − 03	27%	13%	6%	3%	11%	3%	10%
1.425	1.00E − 03	32%	10%	4%	8%	6%	3%	10%
1.425	2.00E − 03	31%	11%	4%	6%	7%	3%	10%
1.425	3.00E − 03	30%	11%	4%	3%	9%	3%	10%
1.425	4.00E − 03	29%	12%	3%	1%	10%	3%	10%
1.425	5.00E − 03	27%	13%	3%	1%	12%	3%	10%
1.450	5.00E − 03	32%	11%	1%	9%	8%	3%	10%
1.450	7.50E − 03	29%	13%	0%	3%	11%	3%	10%
1.450	1.00E − 02	26%	15%	1%	2%	14%	3%	10%
1.500	1.50E − 02	0%	10%	25%	18%	2%	4%	10%
1.525	1.50E − 02	5%	10%	24%	16%	1%	4%	10%
1.550	1.50E − 02	9%	11%	23%	14%	1%	4%	10%
1.575	1.50E − 02	15%	11%	21%	11%	0%	4%	10%
1.550	2.00E − 02	1%	13%	21%	19%	3%	4%	10%
1.575	2.00E − 02	5%	14%	20%	17%	4%	4%	11%

[a]We show the solution space at height bin $l = 6$ (3.12 km). The solution space was identified by combining PA with the results we obtained for effective radius using GCM. BAE1 and BAE2 refer to $\mathring{a}_{\beta(355),\beta(532)}$ and $\mathring{a}_{\beta(532),\beta(1064)}$, respectively.

the solution space of the real and imaginary parts varies between 1.40 and 1.575, and $i0$ and $i0.02$, respectively. We obtain a mean value of $m_R = 1.49 \pm 0.09$ and $m_I = i0.01 \pm i0.01$ [see Table 11 and Fig. 1(e), star].

These levels of uncertainty of the retrieved CRI could be a very valuable result in view of the domains (3) we are working with. For example, in our recent study [16] we observed that we can reduce the total uncertainty of the single-scattering albedo below the measurement uncertainty of the extinction coefficients if we decrease the uncertainty of the imaginary part to 100% or less.

We note that this result for the CRI retrieval can be improved if we have extra information regarding the measurement quality. Our analysis of the structure of the solution space shows that it consists of two subspaces, which can be characterized by

1. $m_R = 1.425 \pm 0.025$, $m_I = i0.005 \pm i0.005$ (see lines which are not highlighted in gray color in Table 4), and

2. $m_R = 1.54 \pm 0.04$, $m_I = i0.0175 \pm i0.0025$ (see lines highlighted in gray color in Table 4).

Both subspaces show similar individual discrepancies of the BAE at 532 and 1064 nm (10%–15%), effective radius (3%–4%), as well as the total discrepancy (10%–11%). However, the two subspaces have quite different individual discrepancies with regards to the lidar ratios and especially the EAE and BAE at 355 and 532 nm, respectively. For example, the discrepancy of the EAE that describes the subspace belonging to $m_R = 1.425 \pm 0.025$ and $m_I = i0.005 \pm i0.005$ does not exceed 7%. In contrast, the discrepancy of the EAE is 20%–25% for the subspace that belongs to $m_R = 1.54 \pm 0.04$, $m_I = i0.0175 \pm i0.0025$. We find an opposite result in the case of the BAE discrepancy. With regards to lidar measurements the BAE at 355 and 532 nm is more robust (lower measurement errors) than the EAE. Therefore, the BAE values allow us to further constrain the solution space and retrieve a more

exact value of the CRI, namely, $m_R = 1.54 \pm 0.04$ and $m_I = i0.0175 \pm i0.0025$.

B. Measurement Case from 3 February 2008

We analyzed the SAMUM measurement from 3 February 2008 [3] in the same way as described in the previous section. Profiles of the OD and the LDP are shown in Figs. 3(a) and 3(b). The retrieval results are shown in Tables 1, 5–7 and Figs. 3(c)–3(f), 4, and 8(b).

This measurement case is very similar to the case from 31 January 2008. There are two distinct aerosol layers. One layer is below 3 km height ($l = 1 - 4$), and the second layer is on top of it ($l = 5 - 12$). The aerosols in the upper layers of both measurements (31 January and 3 February 2008) belong to the same cases 2 and 5 listed in Table 1 of [1]. In contrast, particles in the lower layer of the case from 3 February

2008 are larger than particles in the lower layer of the case from 31 January 2008. We find the cases 5, 6, and 8 (see Table 1), and that puts the effective radius into a radius range of up to 0.4 µm. In both measurement cases we find outliers of the EAE in the highest height bin $l = 12$. These outliers indicate that measurement errors are large. Nevertheless, we use the OD at $l = 12$ in the inversion to check the robustness of the GCM.

Our analysis of the profiles with our simplified PA also shows the presence of a two-layer aerosol system. In that case the lower part of the profiles can be described by a MMS whereas the upper part of the profile can be described by a BMS. The discrepancy $\rho_{LUT,f}$ lies between 2 and 12% at $l = 2 - 4$, and $\rho_{LUT,c}$ is between 2% and 8% at $l = 5 - 11$ (see Table 5). Table 5 shows that the measurement quality of the OD in the lowest height bin ($l = 1$) is not as good
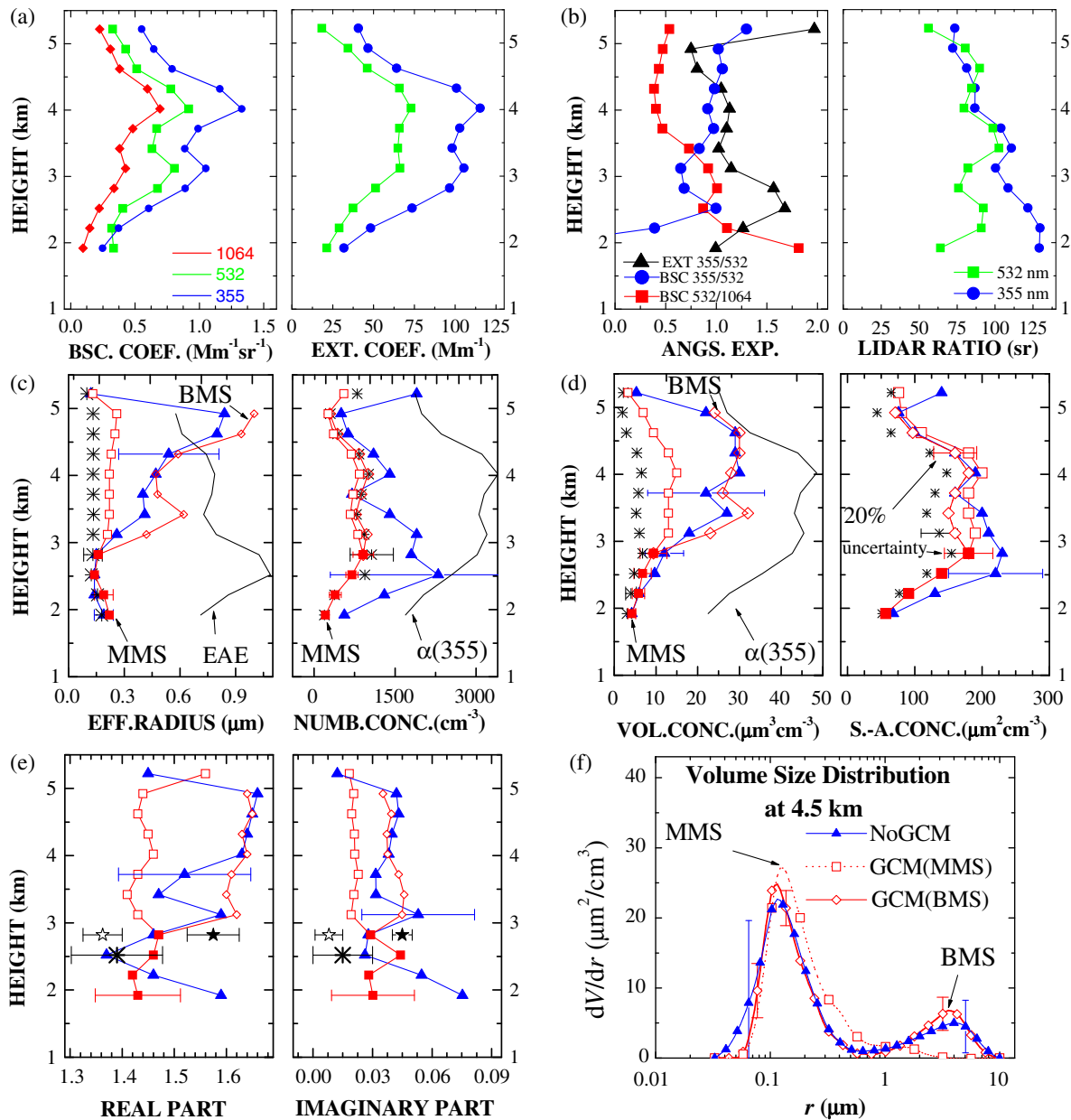

Fig. 3. Measurement case from 3 February 2008. The meaning of the lines, symbols, and colors is the same as in Fig. 1.

Table 5. Measurement from 3 February 2008[a]

l	$\rho_{LUT,f}$	$\rho_{LUT,c}$	$\varphi_{\alpha(355)}$ Fitted from Eq. (23) in [2]	$\varphi_{\alpha(355)}$ Minimization of Eq. (31) in [2]
1	56.6%	—	1	1
2	12.4%	—	1	1
3	3.8%	—	1	1
4	2.0%	—	1	1
5	7.7%	4.5%	0.81	0.90
6	3.9%	2.1%	0.75	0.94
7	8.1%	4.0%	0.79	0.80
8	13.6%	7.8%	0.80	0.80
9	13.9%	7.2%	0.76	0.83
10	11.7%	3.0%	0.63	0.90
11	12.6%	6.2%	0.59	0.87
12	12.5%	—	1	1

[a]The same procedure was applied as explained in Table 2.

as in the highest height bin because $\rho_{LUT,f}^{(1)}$ is very large, that is, 57%. Besides that, the OD set $g^{(1)}$ cannot be split into fine- and coarse-mode particles.

Using PA we find for the fine-mode part of the PSDs in the lower part of the aerosol column the following changes with increasing height. Effective radius decreases from 0.17 to 0.13 µm, the surface-area concentration increases from 51 to 155 µm² cm⁻³, volume concentration increases from 3 to 7 µm³ cm⁻³, and number concentration increases from 191 to 1066 cm⁻³. If we constrain the EAE to $\mathring{a}_{\alpha,f}^{(4)} \approx 1.55$ in the upper part of the profile, the profile of effective radius of the fine mode stays constant at approximately 0.13 µm above 3-km height. Surface-area, volume, and number concentrations of the fine mode change nearly proportionally to the change of the extinction coefficient at $\lambda = 355$ nm. In the upper part of the profile the values of the microphysical parameters are similar to the values in the lower part of the profile [see Figs. 3(c) and 3(d), asterisks]. The fine-mode fractions $\varphi_{\alpha(355)}$ we obtain above 3 km from this method and from our minimization method described by Eq. (31) in [2] are close to 0.85 ± 0.10. The only exceptions are the fine-mode fractions in the highest height bins $l = 10$ and 11, where we find $\varphi_{\alpha(355)} \approx 0.6$ and $\varphi_{\alpha(355)} \approx 0.9$, respectively (see Table 5).

We will now demonstrate how PA can support GCM in a way that allows for a more accurate retrieval of the RCs. We noted before that in contrast to the measurement from 31 January 2008, the measurement case from 3 February 2008 allows for a wider variation of effective radius in the lower

Table 6. Measurement from 3 February 2008[a]

P	a_p MMS (1.5–5.0 km)	b_p	δp	a_p BMS (3.0–5.0 km)	b_p	δp
S	1.9	0	20%	1.6	0	15%
v/r	0.63	0	20%	0.53	0	15%
$n(r_{mean}^2 + \sigma^2)$	0.15	0	20%	0.127	0	15%
r_{eff}	–0.11	0.35	0.05 µm	–1.5	2.2	0.2 µm
σ	0.29	–0.01	20%	0.053	0.03	15%
r_{mean}	0.4	0.05	20%	0.011	0.1	15%

[a]Explanation of how the parameters were obtained is provided in Table 3.

Table 7. Measurement from 3 February 2008[a]

m_R	m_I	Individual Discrepancies ρ_p for: BAE1	BAE2	$\mathring{a}_\alpha$	$\frac{\alpha(355)}{\beta(355)}$	$\frac{\alpha(532)}{\beta(532)}$	r_{eff}	ρ_{LUT}
1.325	1.00E – 03	32%	9%	0%	2%	10%	2%	9%
1.325	5.00E – 04	33%	10%	0%	3%	10%	2%	10%
1.325	1.00E – 03	32%	9%	0%	2%	10%	2%	9%
1.325	2.00E – 03	31%	8%	0%	0%	12%	2%	9%
1.325	3.00E – 03	29%	7%	1%	3%	14%	2%	9%
1.325	4.00E – 03	27%	5%	1%	5%	15%	2%	9%
1.325	5.00E – 03	26%	4%	2%	7%	16%	2%	10%
1.375	1.00E – 02	35%	1%	6%	2%	8%	4%	9%
1.375	1.50E – 02	23%	5%	5%	2%	7%	14%	9%
1.4	1.50E – 02	31%	5%	1%	0%	11%	4%	9%
1.4	1.50E – 02	27%	7%	2%	5%	4%	14%	10%
1.525	4.00E – 02	0%	4%	1%	3%	2%	32%	7%
1.55	4.00E – 02	10%	4%	1%	3%	1%	32%	8%
1.625	4.00E – 02	0%	3%	10%	4%	2%	34%	9%
1.55	4.50E – 02	5%	0%	2%	4%	5%	32%	8%
1.575	4.50E – 02	7%	0%	5%	1%	4%	32%	8%
1.60	5.00E – 02	7%	4%	9%	0%	7%	32%	10%

[a]The solution space at height bin $l = 4$ (2.8 km) was identified in the same way as explained in Table 4.
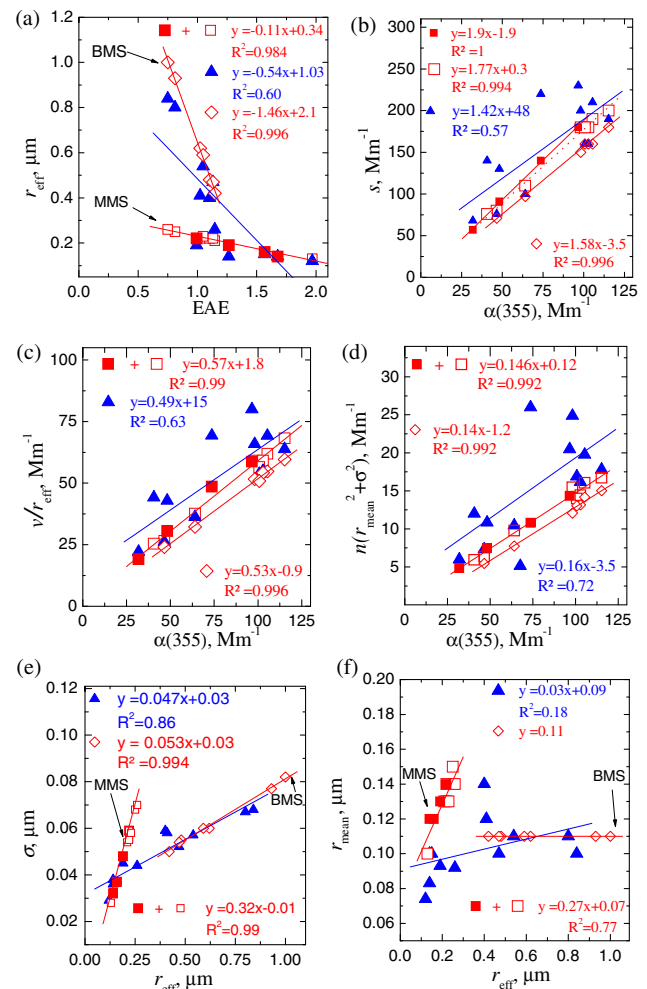

Fig. 4. Measurement case from 3 February 2008. The meaning of the lines, symbols, and colors is the same as in Fig. 1.
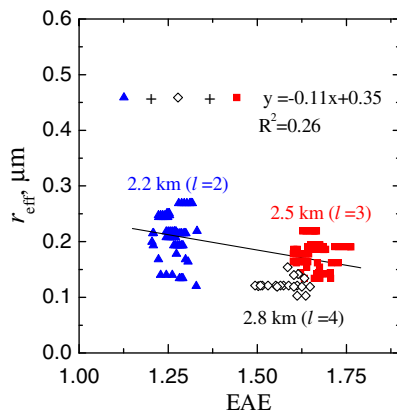
Fig. 5. Effective radius (extracted from our reference LUT) versus measured EAE (3 February 2008) at height bins $l = 2$ (triangles), 3 (squares), and 4 (diamonds). We show the data points (r_{eff}) that are located in the vicinity of the minimal discrepancy $\rho_{LUT,min} = \rho_{LUT,f}$. Parameters of the regression analysis are shown in the legend.

part of the profile. Consequently, there is a larger uncertainty with regard to the selected RC values a_r and b_r. We investigated the properties of the solution space of r_{eff} in dependence of the EAE in the lower part of the profile. For that purpose we collected the LUT elements that are near the minimum discrepancy $\rho_{LUT,min} = \rho_{LUT,f}$ at $l = 2 - 4$ (see Table 1).

Figure 5 shows all elements that fulfill this requirement for the minimum discrepancy. The triangles describe the results for height bin $l = 2$, the squares describe the results for height bin $l = 3$, and the diamonds describe the results for height bin $l = 4$. We find the following equation from these three data sets:

$$y = -0.11x + 0.35,$$

where $a_r = -0.11$ and $b_r = 0.35$. We note that r_{eff} should remain below the line defined by the regression equation if the condition of smoothness of the profiles of the particle properties holds true, that is, small changes of EAE result in proportionally small changes of effective radius in successive height bins. We will come back to this specific feature of the solution space of effective radius when we discuss the results in Section 4.

Figures 3(c)–3(f) show the results retrieved with our traditional technique (NoGCM) and with GCM. The PMPs r_{eff}, n, v, and s obtained with GCM (open squares) and PA (asterisks) agree well in the lower part of the profile (MMS). In contrast, the PMPs r_{eff}, v, and s obtained with GCM and PA are quite different in the upper part of the profile, even in the case of MMS (opened squares). In fact, we do not obtain MMSs from this measurement if we apply MMS in GCM. All PSDs retrieved with MMS above 3 km contain coarse-mode particles. The mode radius is approximately 1.0–1.5 μm; see for example Fig. 3(f), dotted line with squares. These PMPs are overestimated compared to the PMPs obtained with PA.

The use of the two techniques, namely NoGCM and GCM, results in similar effective radii and volume concentrations for this measurement case. We obtain from these two methods larger discrepancies between surface-area concentrations and

especially between number concentrations below 3 km height. We already discussed in the context of the previous measurement case the reasons why outliers occur when we use the traditional technique. The next steps allow us to determine the RCs for GCM. Using the constraints (2a), the OD in the lower part of the aerosol profile are reproduced best after a few iteration steps if $a_s = 1.9$, that is, we simultaneously obtain $a_v = 0.63$ and $a_n = 0.15$. In this case the correlation coefficient is equal to 1 for the lower part of the profile; see Fig. 4(b), closed squares and red solid line. In contrast, the statistics of the solutions we obtain for the upper part of the optical profile are described best by a regression equation for which $a_s = 1.77$; see Fig. 4(b), open squares and dotted line. Furthermore, the OD above 3 km height are not reproduced properly if we try to keep the solutions close to the regression line by means of δs, in which case we would use $a_s = 1.9$. Because of this result we use MMS with RC $a_s = 1.9$, $a_v = 0.63$, and $a_n = 0.15$ for the whole profile from 1.5 to 5.0 km. We use BMS with $a_s = 1.6$, $a_v = 0.53$, and $a_n = 0.127$ above 3 km height. These numbers are in the centers of the respective acceptable ranges; see Table 6.

With regards to the RC a_r, we use for our MMS approach the results we obtained from PA. As we showed before, the linear interpolation of the LUT data in the lower part of the optical profiles works best if we use RC $a_r = -0.11$ and $b_r = 0.35$ (see Fig. 5). In the case of the BMS, we estimate the RCs a_r and b_r based on the analysis of the statistics we obtain for r_{eff} versus $\mathring{a}_\alpha$. We obtain this latter statistic from NoGCM [see Fig. 4(a), blue].

Figure 4(a) shows that the solution space (triangles) is not constrained, that is, the effective radius varies from 0.4 to 0.8 μm for $\mathring{a}_\alpha < 1$. Our goal is that we can estimate the upper limit of effective radius with BMS. We use the RCs $a_r = -1.5$ and $b_r = 2.2$. The respective regression equation results in an effective radius as large as 1 μm at $\mathring{a}_\alpha = 0.5$. The remaining RCs can be found after several iterations using the constraints (2a) and (2b). The final values of the RCs are listed in Table 6, both for MMS and BMS.

The real part of the CRI varies between 1.4 and 1.6 if we use NoGCM. The imaginary part varies between 0.01 and 0.07 along the profile. The profile of the CRI derived with GCM is more stable. The real and imaginary parts obtained with MMS are at the lower boundary of the solution space of the CRI. In contrast, the real and imaginary parts obtained with BMS are at the upper boundary of this solution space [see Fig. 3(e)].

We estimated the CRI at 2.8 km ($l = 4$) from combining PA and GCM. In that height range the PSD is still monomodal and the measurements are comparably accurate ($\rho_{LUT,f} = 2\%$ in this height). Effective radius retrieved with GCM is 0.16 μm. Table 7 shows the LUT elements that are near the minimum discrepancy $\rho_{LUT} = 7\%$ in Eq. (4).

The solution space in that vicinity consists of two subspaces. One of the subspaces is characterized by small individual discrepancies 2%–14% for effective radius and large individual discrepancies 23%–35% for BAE at 355 and 532 nm (see lines which are not highlighted in gray in Table 7). The second subspace in contrast is characterized by large individual

discrepancies 32%–34% for effective radius and low individual discrepancies 0%–10% for BAE at 355 and 532 nm (lines highlighted in gray in Table 7).

This second subspace is represented by LUT elements for which effective radius is approximately 0.12 µm; see also Fig. 5, diamonds. The measurements of the backscatter coefficients are quite accurate, and we believe that the BAE at 355 and 532 nm has comparably lower uncertainties than the retrieved r_{eff}. Thus, we think that the CRI that follows from the results in this second subspace are more trustworthy. We find $m = 1.575 \pm 0.05 - i(0.045 \pm 0.005)$; see Table 11 and Fig. 3(e), closed stars. We note that the first subspace results in $m = 1.36 \pm 0.04 - i(0.008 \pm 0.007)$; see Fig. 3(e), open stars.

C. Measurement Case from 22 January 2008

Figures 6(a) and 6(b) show profiles of OD and LDP taken with lidar on 22 January 2008 [3]. The retrieval results are shown

in Tables 1, 8–10, and Figures 6(c)–6(f), 7, and 8(c). Tables 1 and 8 show that this measurement case is very similar to the previous two measurement cases. Again, we find a two-layered aerosol system. The difference to the previous two cases is that the lower aerosol layer is quite shallow, that is, it occupies one single height bin, namely, $l = 1$. Particle size distributions in the lower part of the profile are monomodal (1.6 km). In the upper part of the profile (1.8–3.5 km) we find bimodal particle size distributions.

We briefly summarize the retrieval results obtained with GCM for this measurement. Effective radius and number, surface-area, and volume concentrations in the lowest height bin are 0.16 µm, 320 cm^{-3}, 67 µm^2 cm^{-3}, and 3.5 µm^3 cm^{-3}, respectively; see Figs. 6(c) and 6(d), red symbols. Effective radius is similar in the upper part of the profile if we use MMS. The other parameters (number, surface-area, and volume concentrations) change proportionally to the profile of $\alpha(355)$. In the
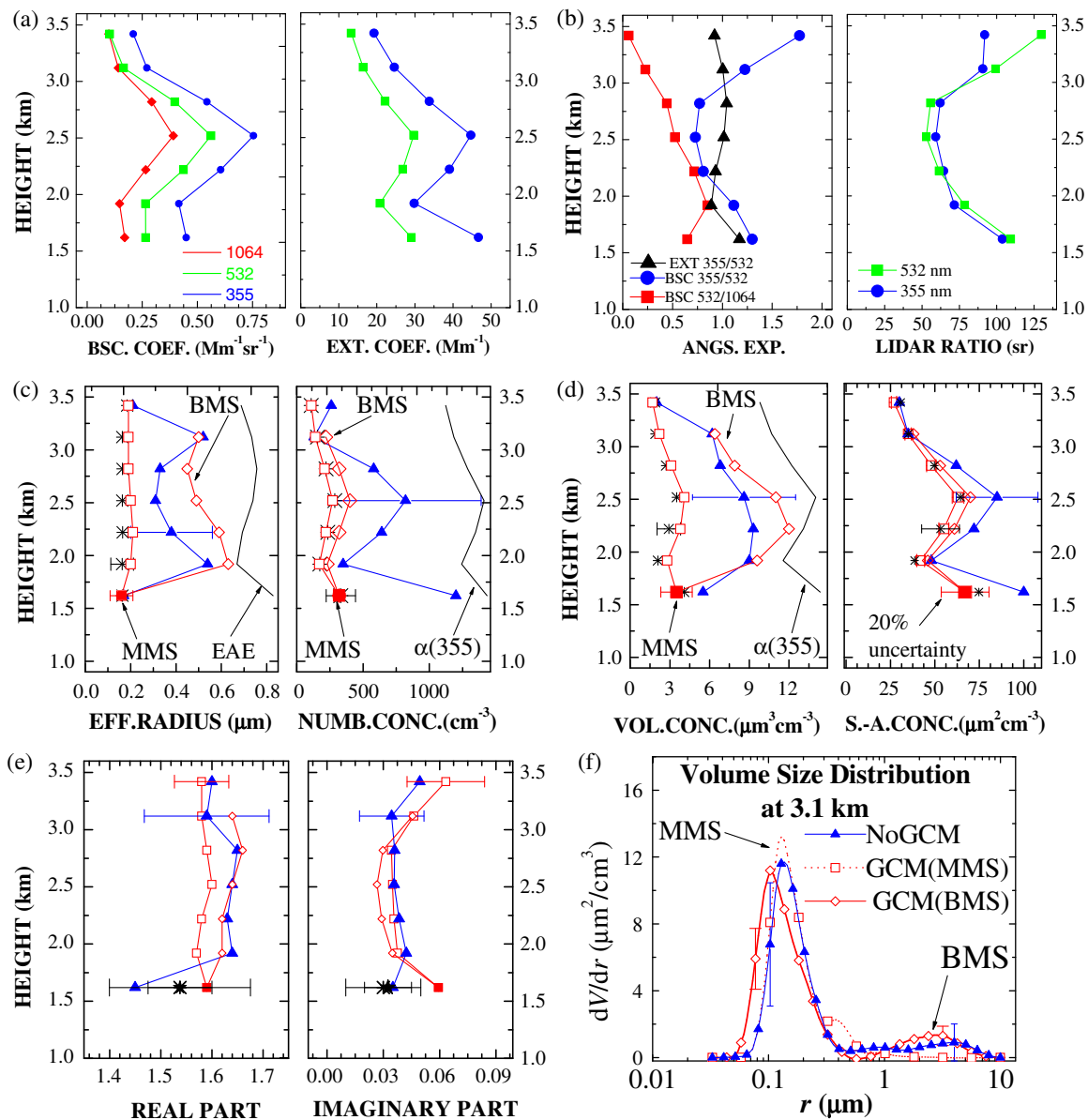

Fig. 6.   Measurement case from 22 January 2008. The meaning of the lines, symbols, and colors is the same as in Fig. 1.

Table 8. Measurement from 22 January 2008[a]

l	$\rho_{\text{LUT},f}$	$\rho_{\text{LUT},c}$	Fitted from Eq. (23) in [2]	Minimization of Eq. (31) in [2]
			$\varphi_{\alpha(355)}$	
1	4.8%	—	1.00	1
2	6.1%	9.3%	0.81	0.75
3	12.9%	4.1%	0.85	0.90
4	20.7%	10.4%	0.90	0.95
5	20.3%	7.1%	0.92	0.85
6	15.0%	9.0%	0.89	0.67
7	21.1%	—	1.00	1

[a]Meaning of the parameters is the same as described in Table 2.

case of BMS, effective radius and volume concentration significantly increase to 0.6 μm and 12 μm³ cm⁻³, respectively, in the upper part of the aerosol profile.

If we retrieve these parameters with PA we find that in the case of the fine mode of the PSD the values agree well to the parameters obtained with GCM/MMS; see Figs. 6(c) and 6(d), asterisks. As in the case of the traditional regularization approach the effective radius retrieved in that way varies between the limits obtained with GCM/MMS and GCM/BMS. We observe a similar behavior for volume concentration, namely, this parameter varies between the limits obtained with GCM/MMS and GCM/BMS. Number and surface-area concentrations retrieved by NoGCM are almost 4, respectively two times larger than the values obtained with GCM in some of the height bins [Figs. 6(c) and 6(d), blue symbols].

The CRI was derived with PA, NoGCM, and GCM. The real part varies between 1.55 and 1.65 along the profile. The imaginary part varies between $i0.03$ and $i0.06$ along the aerosol profile [see Fig. 6(e)]. The only outlier in the profile of the real part obtained with NoGCM is at $l = 1$. If we combine PA and GCM for the retrieval of the CRI at 1.6 km ($l = 1$), we obtain $m = 1.54 \pm 0.06 - i(0.0325 \pm 0.0125)$; see Table 11 and Fig. 6(e), stars.

4. DISCUSSION

In this section we analyze from a statistical point of view the results we obtained from the three case studies and our simulations [2]. We assess in how far our retrieval results are meaningful and whether there are additional patterns in the solution spaces that can be used in GCM and for the quality assurance of the retrieval results. In particular we try to understand

Table 9. Measurement from 22 January 2008[a]

P	a_p	b_p	δp	a_p	b_p	δp
	MMS (1.6–3.5 km)			BMS (1.9–3.1 km)		
S	1.45	0	10%	1.6	0	15%
v/r	0.48	0	10%	0.53	0	15%
$n(r_{\text{mean}}^2 + \sigma^2)$	0.115	0	10%	0.127	0	15%
r_{eff}	−0.12	0.31	0.05 μm	−1.3	1.8	0.2 μm
σ	0.24	0	20%	0.04	0.04	25%
r_{mean}	0.3	0.07	10%	0.05	0.08	10%

[a]Shown are the regression coefficients and the threshold values that were used as constraints in GCM.

Table 10. Measurement from 22 January 2008[a]

m_R	m_I	BAE1	BAE2	$\mathring{a}_\alpha$	$\frac{\alpha(355)}{\beta(355)}$	$\frac{\alpha(532)}{\beta(532)}$	r_{eff}	ρ_{LUT}
		Individual Discrepancies ρ_p for:						
1.475	2.00E − 02	2%	1%	17%	2%	11%	5%	7%
1.475	2.00E − 02	2%	14%	5%	9%	6%	18%	9%
1.475	2.50E − 02	8%	12%	16%	8%	5%	5%	9%
1.475	2.50E − 02	9%	2%	7%	3%	2%	18%	7%
1.500	2.50E − 02	0%	9%	11%	0%	6%	5%	5%
1.500	3.00E − 02	20%	8%	8%	5%	9%	1%	9%
1.525	2.50E − 02	9%	7%	5%	10%	8%	5%	7%
1.525	3.00E − 02	0%	22%	4%	1%	1%	5%	5%
1.525	3.00E − 02	7%	10%	3%	6%	11%	1%	6%
1.550	3.00E − 02	11%	19%	3%	11%	3%	5%	9%
1.525	3.50E − 02	19%	0%	2%	5%	5%	1%	5%
1.550	3.50E − 02	4%	3%	4%	6%	7%	1%	4%
1.550	4.00E − 02	17%	8%	5%	4%	1%	1%	6%
1.575	4.00E − 02	1%	5%	12%	8%	3%	1%	5%
1.575	4.50E − 02	12%	18%	13%	3%	3%	1%	8%
1.600	4.50E − 02	3%	13%	21%	10%	0%	1%	8%

[a]The solution space at height bin $l = 1$ (1.6 km) was identified in the same way as explained in Table 4.
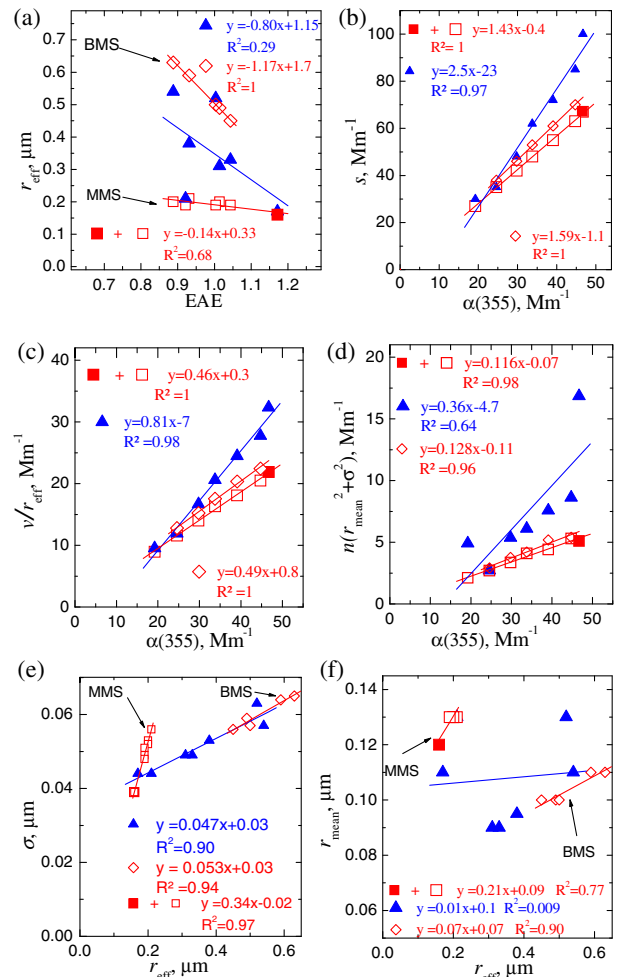

Fig. 7. Measurement case from 22 January 2008. The meaning of the lines, symbols, and colors is the same as in Fig. 1.

Table 11. Retrieval Results of All Three Measurements for the Case of Monomodal PSDs Based on the Combined Use of PA and GCM

Item	31 Jan 2008	3 Feb 2008	22 Jan 2008
Height, km	3.1	2.8	1.6
Case number of Table 1 in [1]	9	6	5
Eff. radius, µm	0.11 ± 0.01	0.14 ± 0.02	0.16 ± 0.03
Real part of CRI	1.49 ± 0.09	1.575 ± 0.05	1.54 ± 0.06
Imaginary part of CRI	0.01 ± 0.01	0.045 ± 0.005	0.0325 ± 0.0125
Lidar ratio (355 nm), sr	67	108	104

if the strong correlation between the profiles of the CRI and the LR is a typical feature [see Figs. 1(b), 1(e), 3(b), 3(e), 6(b), and 6(e)].

We note that total effective radius in one and the same aerosol layer can be either almost constant ($r_{\text{eff}} \approx 0.45$ µm in the upper part of the profile from 31 January 2008) or comparably variable ($r_{\text{eff}} \approx 0.5 – 1.0$ µm in the upper part of the profile from 3 February 2008) despite the fact that the EAE shows a comparably small variation, namely, within 0.7–1.0. Clearly, the set of OD may have measurement errors that could lead to variations of the EAE. However, in the case of bimodal PSDs the total effective radius can significantly change if the EAE varies from 0.7 to 1.0 (see, for example, the stars in Fig. 1(a) of [1]). We analyzed the change of the PSD with height for the measurement from 3 February 2008 to identify possible reasons for the strong variation of effective radius.

Figure 8(b) shows that the PSDs in the different height bins consist of particles in the fine and coarse modes, respectively. The two mode radii are nearly constant, that is, approximately 0.11 and 3.5 µm, respectively. Volume concentration per radius of the coarse mode is approximately 7 µm^3/(µm cm^3) and does not change with height. In contrast, volume concentration per radius interval of the fine mode drops by a factor of two, that is, from 50 to 25 µm^3/(µm cm^3). This change of volume concentration per radius interval of the fine-mode fraction of the PSDs explains the large variation of total effective radius even though the fine-mode and coarse-mode radii stay constant. This case shows that the total effective radius does not describe in a precise and clear manner the PSD. On the contrary, it can even lead to a misinterpretation of the properties of the PSD. In fact, we find that the PSDs $f^{(l)}(r) \approx 0$ at $r \in (0.5; 1.0)$ in Fig. 8(b); that is, there are no particles in this radius range. Simultaneously, the total effective radius of 0.5– 1.0 µm could indicate that PSDs have their maximum at a similar radius range $r \in (0.5; 1)$. In the case of the bimodal PSD the total effective radius merely describes a weighted average of the effective radius of the fine and the coarse mode, respectively. One can show that

$$r_{\text{eff}} \approx \varphi_{\alpha(355)} r_{\text{eff},f} + [1 - \varphi_{\alpha(355)}] r_{\text{eff},c}. \tag{5}$$

Therefore the fine-mode fraction $\varphi_{\alpha(355)}$ and effective radius $r_{\text{eff},f}$ are more valuable pieces of information for the description of the PSD than the total effective radius r_{eff}.

With regards to the measurements from 31 January 2008 the mode radius of the coarse mode of the PSD drops from 4 to 3 µm with increasing height above ground [Fig. 8(a)]. In contrast, the volume concentration per radius increases from 4 to 9 µm^3/(µm cm^3). The decrease of the mode radius of the coarse mode and the simultaneous increase of volume concentration lead to a total effective radius that is almost constant in the upper part of the profile.

In summary, these results show that the total effective radius can change with height as the result of a variation of the particle number concentrations of the fine and/or coarse modes of the PSD, respectively, even if the effective radius of the fine and/or coarse mode remains constant. Some approaches, such as [17], use constraints in which the effective radius of the fine and coarse modes, respectively, are kept constant along the profile, that is, a height-dependence is explicitly excluded. However, we can see from the examples shown in this contribution that there may be situations in which the total effective radius remains constant with height, although the effective radius of the fine and/or coarse mode changes with height. In these cases we need to be careful with our interpretation of the structure of the PSDs and the assumption that (a) profiles of effective radius of the coarse and fine modes are constant and (b) only their number concentrations vary.

We also pay special attention to using GCM for stabilizing the retrieval of the PSD in the radius range from $r_{\text{min}}^{(l)}$ to $r_{\text{max}}^{(l)}$ (see Fig. 8). Despite the size of the search space of the parameters [see Eq. (3a)] the retrieved PSDs do not contain outliers anymore. Such outliers are usually produced if particle radii are less than 0.05–0.075 µm.
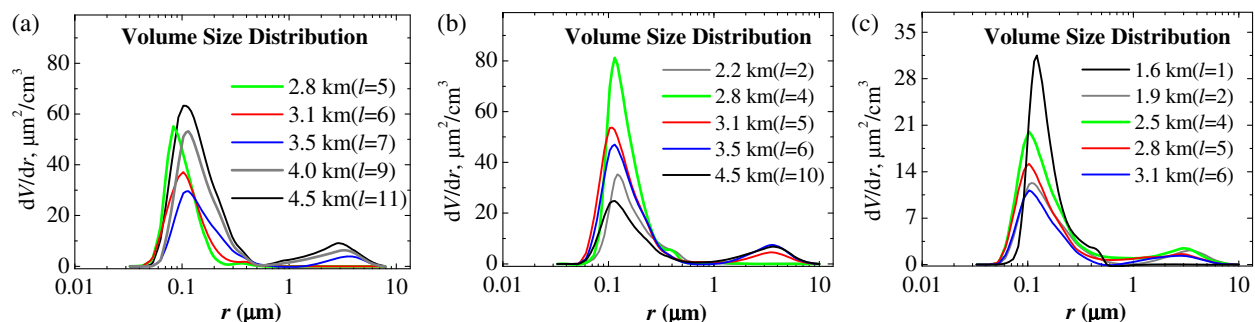

Fig. 8.   Results for PSDs in different height levels. The PSDs were obtained from using GCM. Results are shown for the measurements taken on (a) 31 January 2008, (b) 3 February 2008, and (c) 22 January 2008.
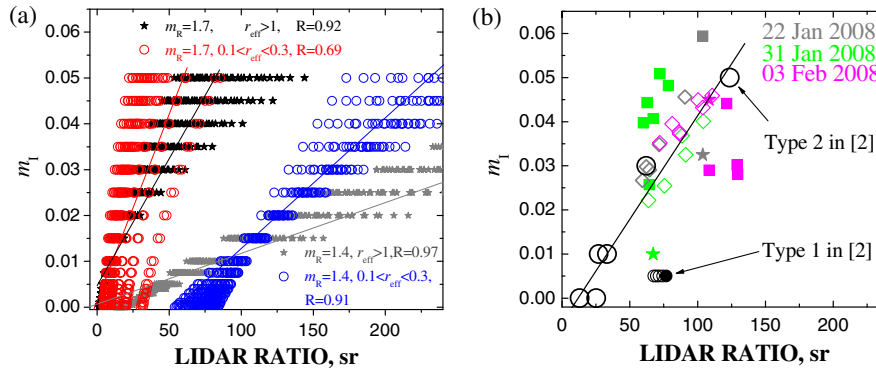
Fig. 9. Statistics of the imaginary part of the CRI versus LR at 355 nm. We show the results we obtained from (a) the LUT and (b) the simulated vertical profiles type 1 (bimodal case) and type 2 (monomodal case) as described in [2] (black circles) and the three measurements: 31 January 2008 (green), 3 February 2008 (pink), and 22 January 2008 (gray).

Last but not least, we discuss the retrieval results of the CRI. For instance, Figs. 6(b) and 6(e) show that the structure of the profiles of the imaginary part retrieved with GCM (red curve) are rather similar to the structure of the profiles of the lidar ratios. We analyzed if this qualitative similarity between the profiles of the imaginary part of the CRI and the lidar ratios is purely coincidental or if there is a physically based reason for this correlation.

It is known from theory that for arbitrary PSD the imaginary part becomes larger (smaller) with increasing (decreasing) lidar ratio if the real part of the CRI is kept at a fixed value [18]. We also find a pattern for the real part versus the lidar ratio. In that case the LR increases with decreasing m_R for constant m_I. We can estimate the degree of this interdependence by means of our LUT. Figure 9(a) presents the results of a statistical analysis of the dependence of m_I versus LR at 355 nm. The results are based on splitting the LUT into four groups of data:

A. particles in the fine mode, namely $r_{eff} \in (0.1\ \mu m; 0.3\ \mu m)$, and high real part of the CRI, namely $m_R = 1.7$ (red symbols);
B. particles in the fine mode, namely $r_{eff} \in (0.1\ \mu m; 0.3\ \mu m)$, and low real part of the CRI, namely $m_R = 1.4$ (blue symbols);
C. particles in the coarse mode, namely $r_{eff} > 1\ \mu m$, and high real part of the CRI, namely $m_R = 1.7$ (black symbols);
D. particles in the coarse mode, namely $r_{eff} > 1$, and low real part of the CRI, namely $m_R = 1.4$ (gray symbols).

The correlation coefficient R increases in these groups from 0.69 (group A) to 0.97 (group D). This result confirms the high correlation between m_I and LR for fixed m_R. The correlation coefficient approaches 1 if variations of the effective radius approach 0. Figure 9(a) also shows that particles with a low real part of the CRI ($m_R \leq 1.4$) cannot be highly light-absorbing (i.e., $m_I \leq 0.01$) if their lidar ratio is less than 100 sr (see blue and gray symbols). On the contrary, particles with a high real part of the CRI (i.e., $m_R \geq 1.7$) are highly light-absorbing ($m_I \geq 0.035$) if their lidar ratio is larger than 75 sr (see black and red symbols). Figure 9(a) illustrates one more interesting phenomenon which explains why lidar ratios exceeding 200 sr are barely possible for atmospheric aerosol particles. Values above 200 sr can only be produced by highly light-absorbing

particles that have a low real part, which to the best of our knowledge of the literature is not realistic.

Finally, we also investigated the interdependence of m_I and LR in our simulated vertical profile of type 1 (bimodal case) and type 2 (monomodal case) in [2]; see here Fig. 9(b), black circles. We do not find a correlation of the data for our type-1 profile. The imaginary part remains constant at $m_I = i0.005$. However, in this case the variations of the LR do not exceed 72 ± 5 sr. In contrast, m_I and LR of our type-2 profile are well correlated.

We stress that similar correlations in our LUT can be found between m_R and LR (not shown here). As we mentioned above, the LR increases with decreasing m_R for constant m_I in this case.

The statistical properties of the solution spaces we described in the previous paragraphs can be used for quality assurance of our CRI retrievals if we use experimental data. Figure 9(b) shows the imaginary parts of the CRI we retrieved with GCM (squares and diamonds) and the imaginary parts we obtained from the combined use of GCM and PA (stars). The data points are plotted versus the measured values of the LRs for the three measurement cases.

We find $m_I^{(8)} = i0.04$ (31 January 2008), $m_I^{(1)} = i0.06$ (22 January 2008) and $m_I^{(6)} = i0.045$ (22 January 2008). The results for the height bins 1 and 2, that is, $m_I^{(1)} = m_I^{(2)} = i0.03$ and LR $= 125$ sr (3 February 2008) could be considered correct if we accept that the sudden drop of the real part of the CRI to a comparably low value of $m_R^{(2)} \approx m_R^{(1)} = 1.43$ is correct. Figure 9(a) furthermore shows that all data points belonging to fine-mode particles with low real part (blue symbols) describe highly light-absorbing particles, namely, $m_I \geq 0.02$. The LR is more than 125 sr in these cases.

However, as we discussed before this combination of high imaginary parts ($i0.03$) and small real parts (1.43) has not been observed so far. Thus, we assume that our results for these two height bins have a high level of uncertainty. Besides, the lowest sections of the profiles of the backscatter coefficients at $\lambda = 355$ and 532 nm cross each other. This crossing of the profiles indicates that the quality of the OD points may not be high in these two height bins $l = 1$ and 2. For these reasons we believe that the changes of the profiles of the imaginary and real parts

of the CRI on 3 February 2008, that is, $m_I = i0.035 \pm i0.01$ and $m_R = 1.5 \pm 0.05$, are more realistic. It means that in this case there still is a correlation between the real part of the CRI and the LR at 355 nm [see diamond in Fig. 3(e) and blue curve in Fig. 3(b)]. From the theoretical point of view such a correlation is possible if the imaginary part is kept constant.

The imaginary parts that belong to the lower part of the profiles taken on 31 January 2008 [closed green squares in Fig. 9(b)] are accumulating at $m_I = i0.0425 \pm i0.0025$ (except for one value at $m_I = i0.025$), that is, we find a slight correlation with LR. However, we believe that this value of $m_I = i0.0425 \pm i0.0025$ overestimates the true value, and that the result derived from the combination of GCM with PA (green stars) is closer to the true value of the imaginary part.

The imaginary parts that describe the upper part of the aerosol profile from 31 January 2008 [green diamonds in Fig. 9(b)] are highly correlated with the LRs. Therefore, if we fix the real part of the CRI to approximately 1.6 at all heights we again observe that the profiles of m_I and LR are correlated to each other [see Figs. 1(b) and 1(e)].

We conclude from our analysis that this interdependence we find between m_I and LR in our three case studies agrees with theoretical estimates and numerical simulations. We will continue with our study of this interdependence. We want to develop a model that provides a quantitative way of describing the connection between the CRI and the measured profiles of, for instance, the LRs, EAEs, and BAEs.

5. CONCLUSION

We presented PMPs of PSDs that were obtained from the inversion of experimental OD taken with multiwavelength Raman lidar on 22 January 2008, 31 January 2008 and 3 February 2008 in the framework of SAMUM [3,4]. The results were obtained from using three approaches, namely, (1) PA of a reference LUT we developed for this study, (2) GCM that uses the constraints (2a)–(2c), and (3) the traditional inversion with regularization. In all three approaches we used our manual inversion software but mimicked the situation as if the software were operated in an unsupervised, automated mode [15].

The most stable and thus most trustworthy profiles of the PMPs are retrieved with GCM. In contrast, our traditional approach of inversion with regularization results in outliers of the PMPs, particularly number and surface-area concentrations, unless we apply extra constraints. These outliers show considerably larger values of number, surface-area, and volume concentrations compared to the values we obtained with GCM. Number concentration is larger by one order of magnitude, surface-area concentration is 5 times larger. Volume concentration is 200% larger.

We find a stable solution space and low uncertainties of number and surface-area concentrations retrieved with GCM. The low uncertainties are explained by the fact that both strategies, namely, BMS or MMS, provide us with similar solutions for these PMPs. As a result, the number and surface-area concentrations can be retrieved with uncertainties less than 50% and 20%, respectively.

If we use GCM for the retrieval of the PMPs we obtain the largest uncertainties of the PMPs in the case of bimodal PSDs.

Effective radius and volume concentration show particularly high uncertainties. The maximum and minimum values of r_{eff} are limited by MMS and BMS. In contrast to n and s, volume concentration is very sensitive to the effective radius of the coarse mode of the PSD. Consequently, a (high) uncertainty of volume concentration is caused by a (high) uncertainty of effective radius. We will explore methods that allow us to further suppress the uncertainties of r_{eff} and v. Reducing the uncertainties will allow for a more careful assessment of the uncertainties of the PMPs of the coarse-mode fraction of the PSDs with PA. One step that could suppress these uncertainties is the extension of the reference LUT to 15 µm.

The fine-mode PMPs (r_{eff}, n, s and v) we obtained from using PA and GCM/MMS agree well at the present stage of our work. The fine-mode PMPs we obtained for the three measurement cases agree within the theoretical uncertainty we use in PA [2]. Furthermore, the combination of PA with GCM allows us to reduce the uncertainty of the CRI of monomodal PSD to as low as ± 0.1 for the real part and to as low as ± 0.01 for the imaginary part, even if we use a wide search range of the real and imaginary part in our data analysis; see Eqs. (3b) and (3c). These levels of uncertainties of the CRI for monomodal PSDs are obtained if the uncertainties of the lidar ratios and the Ångström exponents are less than 10%. Such uncertainty levels, however, pose a challenge for aerosol lidar observations if, at the same time, we want to achieve high temporal and spatial resolutions of the profiles of the PMPs.

The data we obtained from the three cases furthermore showed an almost linear interdependence between the imaginary part of the CRI and the lidar ratio for the fixed real part of CRI. We will continue with our studies of these correlations and try to derive regression coefficients based on different real parts of the CRI.

In the next stage of our development of the GCM and its validation we will use lidar measurements for which *in situ* data are available. A large set of HSRL-2 lidar and *in situ* data acquired by NASA during large-scale campaigns, such as [15], can be found at https://espoarchive.nasa.gov/archive/browse/oracles/.

APPENDIX A: LIST OF ABBREVIATIONS USED IN THE PAPER

Abbreviation	Meaning
BAE	Backscatter-related Ångström exponent
BMS	Bimodal strategy
CRI	Complex refractive index
EAE	Extinction-related Ångström exponent
GCM	Gradient correlation method
LDP	Lidar data product
LR	Lidar ratio
LUT	Look-up table
MMS	Monomodal strategy
NASA	National Aeronautics And Space Administration
NoGCM	Gradient correlation method is not used
OD	Optical data
PA	Proximate analysis
PMP	Particle microphysical parameter
PSD	Particle size distribution
RC	Regression coefficient
SAMUM	Saharan Mineral Dust Experiment

REFERENCES

1. A. Kolgotin, D. Müller, E. Chemyakin, and A. Romanov, "Improved identification of the solution space of aerosol microphysical properties derived from the inversion of profiles of lidar optical data, part 1: theory," Appl. Opt. **55**, 9839–9849 (2016).
2. A. Kolgotin, D. Müller, E. Chemyakin, and A. Romanov, "Improved identification of the solution space of aerosol microphysical properties derived from the inversion of profiles of lidar optical data, part 2: simulations with synthetic optical data," Appl. Opt. **55**, 9850–9865 (2016).
3. M. Tesche, D. Müller, S. Groß, A. Ansmann, D. Althausen, V. Freudenthaler, B. Weinzierl, A. Veira, and A. Petzold, "Optical and microphysical properties of smoke over Cape Verde inferred from multiwavelength lidar measurements," Tellus **63B**, 677–694 (2011).
4. M. Tesche, A. Ansmann, D. Müller, D. Althausen, R. Engelmann, V. Freudenthaler, and S. Groß, "Vertically resolved separation of dust and smoke over Cape Verde using multiwavelength Raman and polarization lidars during Saharan Mineral Dust Experiment 2008," J. Geophys. Res. **114**, D13202 (2009).
5. C. F. Bohren and D. R. Huffman, eds., *Absorption and Scattering of Light by Small Particles* (Wiley, 1983).
6. D. Müller, U. Wandinger, and A. Ansmann, "Microphysical particle parameters from extinction and backscatter lidar data by inversion with regularization: theory," Appl. Opt. **38**, 2346–2357 (1999).
7. I. Veselovskii, A. Kolgotin, V. Griaznov, D. Müller, U. Wandinger, and D. Whiteman, "Inversion with regularization for the retrieval of tropospheric aerosol parameters from multiwavelength lidar sounding," Appl. Opt. **41**, 3685–3699 (2002).
8. C. Böckmann, I. Miranova, D. Müller, L. Scheidenbach, and R. Nessler, "Microphysical aerosol parameters from multiwavelength lidar," J. Opt. Soc. Am. A **22**, 518–528 (2005).
9. D. P. Donovan and A. I. Carswell, "Principal component analysis applied to multiwavelength lidar aerosol backscatter and extinction measurements," Appl. Opt. **36**, 9406–9424 (1997).
10. E. Chemyakin, D. Müller, S. Burton, A. Kolgotin, C. Hostetler, and R. Ferrare, "Arrange and average algorithm for the retrieval of aerosol parameters from multiwavelength high-spectral-resolution lidar/Raman lidar data," Appl. Opt. **53**, 7252–7266 (2014).
11. A. Doicu, T. Trautmann, and F. Schreier, *Numerical Regularization for Atmospheric Inverse Problems* (Springer, 2010).
12. S. Twomey, ed., *Introduction to the Mathematics of Inversion in Remote Sensing and Direct Measurements* (Elsevier, 1977).
13. A. N. Tikhonov and V. Y. Arsenin, eds., *Solution of Ill-Posed Problems* (Wiley, 1977).
14. I. Veselovskii, A. Kolgotin, D. Müller, and D. N. Whiteman, "Information content of multiwavelength lidar data with respect to microphysical particle properties derived from eigenvalue analysis," Appl. Opt. **44**, 5292–5303 (2005).
15. D. Müller, C. A. Hostetler, R. A. Ferrare, S. P. Burton, E. Chemyakin, A. Kolgotin, J. W. Hair, A. L. Cook, D. B. Harper, R. R. Rogers, R. W. Hare, C. S. Cleckner, M. D. Obland, J. Tomlinson, L. K. Berg, and B. Schmid, "Airborne multiwavelength high spectral resolution lidar (HSRL-2) observations during TCAP 2012: vertical profiles of optical and microphysical properties of a smoke/urban haze plume over the northeastern coast of the US," Atmos. Meas. Tech. **7**, 3487–3496 (2014).
16. A. Kolgotin, E. Chemyakin, A. Romanov, and D. Müller, "Influence of the uncertainty of the imaginary part of the refractive index on the retrieval accuracy of particle scattering and absorption coefficients and single scattering albedo: numerical simulations for the case of multiwavelength Raman lidar data," *Proceedings of ILRC*, Porto Heli, Greece, 26 June, 2012, pp. 269–272.
17. J. Wagner, A. Ansmann, U. Wandinger, P. Seifert, A. Schwarz, M. Tesche, A. Chaikovsky, and O. Dubovik, "Evaluation of the lidar/radiometer inversion code (LIRIC) to determine microphysical properties of volcanic and desert dust," Atmos. Meas. Tech. **6**, 1707–1724 (2013).
18. J. Ackermann, "The extinction-to-backscatter ratio of tropospheric aerosol: a numerical study," J. Atmos. Ocean. Technol. **15**, 1043–1050 (1998).